A novel, well-resolved direct laser bioprinting system for rapid cell encapsulation and microwell fabrication

Zongjie Wang[1,#], Xian Jin[1,#], Zhenlin Tian[2], Fred Menard[2], Jonathan F. Holzman[1,*],

Keekyoung Kim[1,3,*]

[1]School of Engineering, University of British Columbia, Kelowna, BC, V1V 1V7, Canada

[2]Department of Chemistry, Irving K Barber School of Arts and Sciences, University of British

Columbia, Kelowna, BC, V1V 1V7, Canada

[3]Biomedical Engineering Program, University of British Columbia, Vancouver, BC, V6T 1Z4,

Canada

#: These authors contributed equally to this work.

*Corresponding authors:

Dr. Jonathan F. Holzman, email: jonathan.holzman@ubc.ca

Dr. Keekyoung Kim, email: keekyoung.kim@ubc.ca

Abstract

A direct laser bioprinting (DLBP) system is introduced in this work. The DLBP system applies visible-laser-induced photocrosslinking at a wavelength of 405 nm using the photoinitiator VA-086. It is shown that such a system can fabricate vertical structures with fine features (less than 50 µm), and high cell viability (greater than 95%). Experimental characterizations and theoretical simulations are presented, with good agreement seen between the experiments and theory. The DLBP system is applied to the fabrication of (1) cell-laden hydrogel microgrids, (2) hydrogel microwells, as well as a test of (3) cell encapsulation, and (4) cell seeding. The DLBP system is found to be a promising tool for bioprinting.

Introduction

Studies in recent years have shown that *in vitro* cells behave more like their *in vivo* counterparts when they are cultured in a 3D environment rather than as typical plated monolayers.[1–3] Indeed, cellular activity—stem cells fate;[4–6] cancer cells development[7,8]—is highly sensitive to chemical, mechanical, and biological conditions of the 3D environment (e.g., growth factors, matrix stiffness, ion density). Accordingly, a major challenge for bioengineers remains the creation of 3D platforms for cell culture that can adequately mimic their native 3D environment.

The most common 3D platforms are organ-on-a-chip systems[9,10] and bioprinted tissues.[11,12] Organ-on-a-chip systems are microfluidic devices with perfusable chambers containing living cells. Great care is required to fabricate these systems in a biomimetic manner that can achieve tissue-like physiology *in vitro*.[13–16] The drawbacks of this microfabrication technology include practicality (cost, processing time) and performance (heterogeneity, complexity). Thus, organ-on-a-chip systems have not seen widespread implementation, [13,17] and bioprinted tissues have emerged in response to these limitations. Bioprinted tissues are created by an automated biocompatible 3D printing process: it assembles biomaterials and cells into complex 3D scaffolds that closely mimic the *in vivo* 3D environment.[11,18] Interest in bioprinting has increased greatly over the past few years because the technique can produce biomimetic 3D tissues in a rapid and cost-effective manner.

There are many techniques for bioprinting, the most popular being extrusion-based bioprinting.[18] Extrusion-based bioprinting involves depositing a mixture of cells and biomaterials

as a fluid using a pneumatic dispensing system. While the technique is simple and has been used to fabricate many complex cell-laden structures,[19–25] it suffers from feature resolutions limited to 300–500 μm,[19–25] and poor cell viability (≤ 80%).[11,18,26,27] It has been recently reported that applying voltages (> 1000 V) between the nozzle and printing plate can improve the resolution of extrusion-based bioprinting to 80 μm without significant decreases in cell viability.[28] Yet, this modification is still only feasible for an alginate/Ca^{2+} gelation. A second technique is inkjet bioprinting.[29,30] Inkjet bioprinting dispenses biomaterials as droplets and is as simple as extrusion-based bioprinting. However, a major drawback of inkjet bioprinting is its inability to create 3D structures with vertical features. A third technique is laser-induced forward transfer (LIFT) bioprinting.[31–33] The process involves irradiating a small area of an absorbing layer to generate a bubble, thereby causing a cell suspension to form a droplet that is then collected by a receiving plate. LIFT has excellent cell viability (> 95%), but it requires a complicated setup: a high power laser source, a custom energy-absorbing layer, and a suspension of cells and biomaterials under the absorbing layer. A fourth technique is light/radiation-based bioprinting: visible or ultraviolet (UV) light shapes photocrosslinkable biomaterials into complex 3D structures. Stereolithographic bioprinting is now the most popular light/radiation-based bioprinting technique. It uses a projected light pattern to print patterns one layer at a time. Stereolithographic bioprinting is advantageoulsy compatible with standard stereolithographic equipment, but its suffers from low feature resolution when using visible light (> 500 μm),[34,35] or it can lead to mutagenic and carcinogenic effects whe using UV light. While an option is to seed cells after stereolithographic bioprinting, it prevents true 3D cell-embedded culture.[36,37]

In an attempt to alleviate the challenges of current bioprinting systems, we introduce a new subcategory of light/radiation-based bioprinting: direct laser bioprinting (DLBP). Our DLBP system is shown in Figure 1A. DLBP's rapid photocrosslinking enables the creation of complex 3D structures. In this system, photocrosslinking occurs by combining a highly reactive, biocompatible photoinitiator to a 405 nm continuous-wave laser. A systematic characterization was carried out using poly(ethylene glycol) diacrylate (PEGDA) as a hydrogel biomaterial. We found that the photocrosslinking process was extremely selective: fine feature resolutions of less than 50 μm were achieved. The photocrosslinking process was analyzed with a model of visible-laser-induced photocrosslinking and polymerization, and the model shows good agreement with the characterization. The applicability of the DLBP system was demonstrated by bioprinting cell-laden hydrogel microgrids and hydrogel microwells. With microgrids, cell encapsulation leads to > 95% cell viability. With microwells, adhesion of MCF-7 cells to the hyrdogel depends on the wells' size and interfaces. Overall, the DLBP system provides a promising tool for tissue engineering.

Results

Characterization of the DLBP system

The design of the DLBP system is shown as a 3D schematic in Figure 1A. A photograph of the actual setup is also given in Figure S1. In order to investigate the capability of the system, we first characterized the minimum feature size that the DLBP system could print, which is set predominantly by the size of the laser beamspot. It was measured using the modified setup of standard razor edge technique for characterizing beam profiles (Figure S2A).[38] The resolution of

the measurements was found to be approximately 1 µm, according to observations of edge roughness in scanning electron microscope (SEM) images (Figure S2B to S2D). Characterization of a representative laser beamspot is shown in Figure 1B. The figure shows the laser beamspot size (i.e., the full-width-at-half-maximum (FWHM) of the intensity profile) as a function of height (i.e., the vertical position of the razor edge along the z-axis). With this arrangement, focusing could be applied at heights between $z = -250$ µm and $z = +250$ µm with a laser beamspot size of fewer than 40 µm.

We further optimized bioprinting parameters of the DLBP system for bioprinting of hydrogels in two experiments. The first experiment, shown in Figure 1C (upper), created a crosslinked hydrogel pattern on a non-adhesive substrate when the laser beamspot was focused within the PEGDA prepolymer solution. Various hydrogel patterns were created with this implementation. Representative hydrogel patterns, using a stage velocity of $v = 2.5$ mm/s and optical power of $P = 6$ mW, are shown as meshes in the SEM images of Figure 1D. It is noted that the applied parameters lead to noticeably vertical sidewalls. The observed high aspect ratio was a result of the high selectivity of the photocrosslinking process and the long depth of focus of the laser beam, which established sufficient optical intensity to initiate photocrosslinking within the long cylindrical profile of the focused laser beam. The minimum feature size that could be printed using this technique was 40 µm, which agreed with the laser beamspot characterization described above. It is important to note that the hydrogel patterns created by this first experiment did not remain fixed in place during post-printing handling.

The second experiment, shown in Figure 1C (bottom), created a crosslinked hydrogel pattern

that was fixed in place on a chemically functionalized glass slide. The glass slide was coated with 3-(Trimethoxysilyl)propyl methacrylate to covalently bond the printed hydrogel on its surface during photocrosslinking that is initiated by the focused laser beamspot. Various fixed hydrogel patterns were created in this experiment, having a stage velocity of $v = 2.5$ mm/s and optical power of $P = 6$ mW. They are shown as 'UBC' patterns in Figure 1E. The hydrogel patterns in these SEM images exhibited vertical sidewalls, as is typically desired, however, their minimum feature size has increased to approximately 70 μm. The underlying cause of the increased minimum feature size is unclear, but it is likely due to reflections off the surfaces of the coated glass slide, which lead to back-reflected beams in the PEGDA prepolymer solution and increased feature sizes.

A characterization was also carried out to quantify the effects of stage velocity, v, and optical power, P, on printed hydrogel lines. Figure 2A shows representative SEM images of hydrogel lines for a stage velocity of $v = 1.5$ mm/s with an optical power of $P = 11$ mW (left), a stage velocity of $v = 2.5$ mm/s with an optical power of $P = 11$ mW (middle), and a stage velocity of $v = 2.5$ mm/s with an optical power of $P = 6$ mW (right). A comparison between the left and middle figures shows that an increasing stage velocity decreases the hydrogel line width, while a comparison between the middle and right figures shows that a decreasing optical power decreases the hydrogel line width. Such observations come about because both the increasing stage velocity and decreasing optical power reduce the optical fluence (i.e., the accumulated optical energy per unit area) which leads to a decreased hydrogel line width.

To gain a quantitative understanding of the visible-laser-induced photocrosslinking, the hydrogel lines were characterized for various stage velocities and optical powers. The results,

shown in Figure 2B, plot the hydrogel line width, w, as a function of the stage velocity, v, for

optical powers of $P = 6$, 9, and 11 mW. Results are not shown for a stage velocity of $v = 2.8$ mm/s

with optical powers of $P = 6$ and 9 mW because these conditions did not reliably form hydrogel

lines. The displayed results clearly show that the hydrogel line width decreases as the stage velocity

increases and the optical power decreases.

Bioprinting of cell-laden hydrogel microgrids

Cellular encapsulation is one of the most important applications for this technology. Thus, the

DLBP system was used to print cell-laden hydrogel microgrids and cell viability was then

quantified. The microgrids were formed with MCF-7 cells encapsulated within hydrogel lines. The

hydrogel lines were fabricated with four combinations of stage velocities and optical powers ($v =$

0.5 mm/s and $P = 11$ mW, $v = 0.5$ mm/s and $P = 6$ mW, $v = 1.5$ mm/s and $P = 6$ mW, and $v = 2.5$

mm/s and $P = 6$ mW) which yielded hydrogel line widths of $w = 420$, 270, 160, and 80 μm,

respectively.

Figure 3A displays images of the cell-laden microgrids in four columns: the first column

shows phase-contrast images; the second column shows fluorescent images of live (green) and

dead (red) cells; the third column shows merged images of phase-contrast and fluorescent images.

The cells were clearly encapsulated within the crosslinked hydrogels with a predominance of live

cells within the crosslinked hydrogels. This suggests that the DLBP system is capable of printing

cells with high viability. Figure 3B shows the cell viability for the applied stage velocities and

optical powers. The average cell viability of the DLBP system was approximately 95%, and the

difference in cell viability for the various stage velocities and optical powers was not statistically significant.

The DLBP system is found to be successful in bioprinting cell-laden hydrogel microgrids. The feature resolution was below 100 μm, which outperformed many of the resolutions for contemporary bioprinting techniques,[18] while the average cell viability of 95% is comparable to those of highly-biocompatible inkjet and laser-induced bioprinting techniques.[11,18]

Bioprinting of hydrogel microwells

Cellular seeding was demonstrated with the DLBP system to fabricate hydrogel microwells. Subsequent cell proliferation and migration were measured. The fabrication used stage velocities of $v = 0.5$, 1.5, and 2.5 mm/s and a power of $P = 6$ mW to create microwells with side-lengths of $a = 460$, 340, and 270 μm, respectively. The microwells were created with and without 0.1% gelatin coating. MCF-7 cells were seeded on the microwells, and cell viability test was carried out on day 3.

Figure 4A shows images of the microwells in three columns: the first column shows phase-contrast images; the second column shows fluorescent images of live (green) and dead (red) cells.; the third column shows merged images. Figure 4B shows the results for cell confluency, as the percent coverage of the microwell area by cells. Figure 4C shows the results for the uniformity of the cell distribution. First, comparisons of the images in the first three rows of Figure 4A, and the first three bars of Figure 4B, show that cell proliferation was promoted and thus cell confluency was increased by reducing the size of the microwells. When the side-lengths were reduced from a

= 460 μm to a = 340 μm to a = 270 μm, the cell confluency was increased from 13% to 17% to 25%. Second, comparisons of the images in the second and fourth rows of Figure 4A, and the second and fourth bars in Figure 4B, show that cell proliferation was promoted and thus cell confluency was increased by applying a gelatin coating. The introduction of the gelatin coating increased the cell confluency from 17% to 46%. Such an observation agrees with the findings of prior studies.[39,40] It is worth noting here that applications of microwells typically demand adhesion to the bottom (glass) surface, with minimal adhesion to the vertical (PEGDA) sidewalls. The gelatin coating met this demand because it promoted adhesion to the bottom (glass) surface while maintaining the non-adhesive characteristic of vertical (PEGDA) sidewalls. Such a finding is advantageous because it can allow the gelatin coating to be used for simple single-step promotion of cell proliferation.

Cell migration was also examined at Day 3. First, it is noted that the fluorescence intensity from cells outside the microwells was extremely low, at less than 5% of the maximum intensity, which agrees with prior findings that the adhesion was low between cells and the PEGDA sidewalls.[41,42] Second, comparisons of the images in first three rows of Figure 4A, and the first three bars of Figure 4C, show that cell migration was inhibited and thus the uniformity of the cell distribution was increased by reducing the size of the microwells. When the side-lengths were reduced from a = 460 μm to a = 340 μm to a = 270 μm, the uniformity of the cell distribution increased from 10% to 66% to 77%. Moreover, comparisons of the images in the second and fourth rows of Figure 4A, and the second and fourth bars in Figure 4C, suggest that the gelatin coating has a strong effect on the cell migration and thus uniformity. The uniformity of the cell distribution

increased from 66% to 97% when the gelatin coating was introduced. Overall, the DLBP system was successful in bioprinting hydrogel microwells. The physical characteristics of the microwells could be tailored via size and interfaces to promote cell proliferation and migration. The findings motivate future studies applying size-dependent formation and differentiation of embryonic stem cell bodies[40,43] or cancer cell spheroids.[44]

Optimization of the DLBP system

The plotted results in Figure 5A and 5B clearly show that the hydrogel line width decreases as the stage velocity increases and the optical power decreases. This occurs because higher stage velocities and lower optical powers yield lower optical fluences over the Gaussian profile of the laser beamspot, which leads to reduced areas over which the optical fluence meets the threshold needed to create a sufficiently dense hydrogel network. Such observations are interpreted via an optical fluence model in the following discussion.

A simple optical fluence model is applied here to characterize the optical fluence, in terms of the stage velocity, v, and optical power, P, and relate this optical fluence, Φ, to the hydrogel line width, w. The laser beamspot is assumed to have a Gaussian intensity profile with a FWHM of $2(\ln(2))^{1/2} r_0$, where r_0 is the radius at which the intensity drops to e^{-1} of its peak intensity and the total optical power across the intensity profile is P. The laser beamspot is applied to the plane of the sample, which is defined by x- and y-dimensions. It is actuated at a constant velocity of v along the y-axis and is symmetric about $x = 0$. Thus, for a laser beamspot with an optical power of P, the intensity (in units of mW/mm^2) at the position (x,y) at time t is

$$I(x, y, t) = \frac{P}{2\pi \ln(2)r_0^2} \exp(-(x^2 + (y - vt)^2)/r_0^2) = I_0 \exp(-(x^2 + (y - vt)^2)/r_0^2), \quad (1)$$

where I_0 is defined as the peak intensity. The intensity contributes to a differential optical fluence,

$d\Phi(x) = I(x,y,t)dt$, being the increase in optical energy per unit area during the differential time

period of dt. Thus, the total optical fluence (in units of mJ/mm^2) applied at the position (x,y) under

a steady-state condition (i.e., spanning all time) is

$$\Phi(x) = \frac{P}{2\pi \ln(2)r_0^2} \exp(-x^2/r_0^2) \int_{-\infty}^{+\infty} \exp(-(y - vt)^2/r_0^2)dt = \frac{P}{2\pi \ln(2)r_0^2} \frac{\sqrt{\pi}\,r_0}{v} \exp(-x^2/r_0^2),$$
$$\Phi(x) = \Phi_0 \exp(-x^2/r_0^2), \quad (2)$$

where Φ_0 is the peak optical fluence occurring along the $x = 0$ line. The optical fluence seen in

equation (2) establishes the photocrosslinking.

The measured hydrogel line width, w, is shown as a function of the peak optical fluence, Φ_0,

in Figure 5A. Two things are apparent from the measured hydrogel line widths (blue dots) in the

figure. First, there is a threshold optical fluence, Φ_{th}, below which the laser beamspot does not

initiate sufficient photocrosslinking to form a hydrogel line. Only when the peak optical fluence is

at or above this threshold optical fluence, a sufficiently dense hydrogel network is established and

a hydrogel line is formed (i.e., $w(\Phi_0 \geq \Phi_{th}) \geq 0$). Second, for peak optical fluences above the

threshold, the hydrogel line width increases via a sublinear trend with the peak optical fluence.

This sublinear trend is the manifestation of the aforementioned threshold within the Gaussian

function of equation (2). The outer edges of the hydrogel line, at $x = \pm w/2$, are points at which the

optical fluence drops to its threshold (i.e., points at which $\Phi(x = \pm w/2) = \Phi_{th}$). Thus, hydrogel lines

are formed with widths of $w = w_0 (\ln(\Phi_0/\Phi_{th}))^{1/2}$. This expression is displayed as a curve-fit (blue

line) in Figure 5A, with the curve-fit parameter Φ_{th} being the threshold optical fluence and the curve-fit parameter w_0 being a characteristic width that is proportional to r_0. The curve-fit yields parameters of $\Phi_{th} = 30.6$ mJ/mm^2 and $w_0 = 140.4$ μm.

The curve-fit for the optical fluence model shows good agreement with the measured data points. The coefficient of determination for the curve-fit is $R^2 = 0.958$. However, the parameter w_0 is larger than the value of $2r_0$ that would be expected from a linear manifestation of visible-laser-induced photocrosslinking. In this system, there appears to be some level of saturation in the process—likely due to the finite number of monomers that are available for polymerization. With this in mind, the following discussion introduces a photochemical model to characterize the process of visible-laser-induced photocrosslinking.

The photochemical model is developed to analyze the complete process from laser excitation to polymerization. The model balances the numbers of uncrosslinked and crosslinked monomers within the system with the consideration of the fact that the total number of monomers must remain constant. The concentrations (in units of monomers/mm^3) are denoted by [M] for the uncrosslinked monomers, [M$_i$] for the crosslinked monomers, where the integer i signifies the number of crosslinked monomers within the polymer chain, and [M$_{tot}$] for the total number of monomers. These concentrations are linked by the expression

$$[\text{M}] + \sum_{i=2}^{\infty} i \times [\text{M}_i] = [\text{M}_{\text{tot}}] . \tag{3}$$

After a rigorous derivation, described in the supplementary information, the concentration of crosslinked monomers in polymer chains, [N(x,y,t)], can be found as a function of position (x,y)

and time t. This concentration $[N(x,y,t)]$ can be defined in terms of $[M_{tot}]$ by the expression

$$[N(x, y, t)] = [M_{tot}]\left(1 - \exp\left(-\frac{\sqrt{\pi I_0}\, k_0 r_0}{\sqrt{2}v}\exp(-x^2/(2r_0^2))\left(1 - \mathrm{erf}\left(\frac{y - vt}{\sqrt{2}r_0}\right)\right)\right)\right). \qquad (4)$$

Simulations were carried out to visualize the results of the photochemical model with MATLAB 2015b software (Mathworks, Natick, MA, USA). The simulation results were also used to characterize the relationship between the hydrogel line width, w, and the stage velocity, v, and optical power, P, as shown in Figure 5A and 5B. Equation (4) is applied with the threshold concentration, $[N_{th}]$. Figure 5C shows the concentration of polymer chains, $[N(x,y,t)]$, as a colourmap for the laser beamspot traveling along the y-axis while centered about $x = 0$. The regions above this threshold concentration, being $[N_{th}] = 100$ on the normalized scale, that are considered as the area being photocrosslinked, are shown in blue. The simulations use stage velocities of $v =$ 2.8, 2.5, 2.0, 1.5, 1.0, and 0.5 mm/s and an optical power of 6 mW. The concentration is shown on a normalized scale of 100. In accordance with the measurements, the threshold concentration needed to establish a sufficiently dense hydrogel network and form a hydrogel line occurs for a stage velocity of 2.8 mm/s and an optical power of 6 mW.

The conditions applied earlier for the measured hydrogel lines were applied to simulations. The simulated and measured results are shown in Figure 5B. The figure shows the hydrogel line width, w, as a function of the stage velocity, v (excluding the 0.5 mm/s), for an optical power of 6 mW. It can be seen that there is good agreement between the simulations and measurements. (Although it is not shown, good agreement (within $\pm 10\%$) is also found for the results with optical powers of 9 mW and 11 mW.) The simulation results are also presented for a comparison

between the hydrogel line width, w, and the peak optical fluence, Φ_0. These results, shown in Figure 5A, also show good agreement (within $\pm 8.7\%$). It is worth noting that the simulated and measured results show especially strong agreement when the stage velocity and optical power are above the threshold condition, as the threshold condition has the hydrogel lines being on the verge of formation. When the stage velocity and optical power are kept above the threshold condition, the simulated and measured hydrogel line widths show especially strong agreement (within $\pm 4.6\%$).

Discussion

Photocrosslinking of the DLBP system

Photocrosslinking utilizes a light, which decomposes a photoinitiator to form free radicals, for crosslinking a pre-polymer solution with the phoiniator into a polymer hydrogel network. The proposed DLBP system implements this photocrosslinking process while considering two key metrics: cell viability and feature resolution.

To have photocrosslinking achieve the desired high cell viability, three conditions must be met. First, the light source should be selected to minimize UV-induced mutagenesis or carcinogenesis of cells.[45] Thus, it is preferable to use a light source emitting in the visible range (i.e., wavelength above 400 nm). Second, the chemical photoinitiator should be biocompatible and have low cytotoxicity. Most popular photoinitiators, such as Irgacure 184 and Irgacure 651,[46] or cationic photoinitiators generate cytotoxic byproducts during the chemical reaction.[47] Third, a

short photocrosslinking time is crucial because cell viability decreases rapidly with irradiation time.[48]

To achieve fine feature resolution, two conditions must be met. First, the photoinitiator should be highly chemically selective upon activation. Such chemical selectivity ensures that only the desired functional groups react, and do not trigger a free-radical crosslinking cascade that polymerizes a volume larger than intended. Second, the light source should be capable of delivering light in a well-defined spatial domain. This spatial control is essential to confine rigidification to the small area targeted and to achieve fine spatial design.

Given the above considerations for cell viability and resolution, the developed DLBP system is based upon photocrosslinking with the photoinitiator 2,2'- azobis[2- methyl- n- (2- hydroxyethyl) propionamide] (VA-086) as described in Figure 6 and a visible (GaN-based) laser diode with precise focal characteristics. The selected VA-086 photoinitiator for our DLBP system is a water-soluble azo-based photoinitiator. It shows low cytotoxicity, up to 1.5% w/v concentration, and its cell viability after encapsulation is better than those reported for other widely used photoinitiators.[49] Following laser excitation, it decomposes into an inert gas (N_2) and free radicals. The free radicals trigger the chain polymerization of monomers containing acrylates, which forms the hydrogel network. The laser excitation and polymerization process are shown in Figure 6A. The optical absorption characteristics for the photoinitiator VA-086 in the PEGDA prepolymer solution are shown in Figure 6B. The absorption spectrum of the photoinitiator shows a maximal absorption efficiency at approximately 370 nm, yet its absorption extends above the UV range, up to approximately 415 nm, at which point its absorption is 10% of the peak value. Thus, a light

source with a wavelength between 400 nm and 415 nm should still be able to initiate photocrosslinking and avoid the deleterious effects of UV illumination for cells.[45]

The selected light source for our DLBP system is a visible (GaN-based) laser diode. The spectral power density of the laser is shown as normalized optical power characteristics in Figure 6C. The laser exhibits maximal emission at 405 nm, which is well suited to the optical absorption characteristics of the VA-086 photoinitiator. It is important to note that the laser is used with a microscope objective having a long working distance (and thus long focal length), for focusing deep into the PEGDA prepolymer solution, and a moderately high numerical aperture, for focusing down to a sufficiently small laser beamspot. In our prior studies with a similar laser diode, we found that microscope objectives with shorter working distances and lower numerical apertures led to unacceptably long photocrosslinking times, e.g., 10 seconds range.[50]

Cell viability after encapsulation of the DLBP system

Since building 3D cancer model *in vitro* is highly demanded for cancer research,[51] we chose the breast cancer cell line, MCF-7, to demonstrate the capability of the DLBP system for future cancer research applicaions. Cell proliferation is regulated by both the size and interface of the microwell. In general, a microwell that closely mimics the cell's native microenvironment will support its proliferation. This is a particularly important point for studies that exploit cell differentiation, such as those based upon embryonic stem cells,[42,52] where the size of the microwell plays a central role in defining cell fate. In this study, cell proliferation within a microwell was characterized by cell confluency, and it was quantified by the percent coverage of the microwell area by cells. Cell

migration is regulated mainly by both the size and interfaces the microwell. It can be an important property to control in applications seeking cell spheroids[41,42,52–54] or monolayers[55,56]. Cell migration was characterized by the uniformity of the cell distribution within a given microwell[57]. The cells were seeded with a homogeneous dispersal. Thus, a final cell distribution with clustering on the perimeter of the microwell (i.e., low uniformity) would be the indication of substantial migration, while a final cell distribution that is largely homogenous (i.e., high uniformity) would be the indication of little migration. Uniformity of the cell distribution was computed via the quadrant-based method[58], as described in the Materials and Methods Section.

The proposed DLBP technique can be modified according to needs for mechanical properties and cell culturing. The PEGDA hydrogel that was used in this study has a low molecular weight (700 Da) with strong mechanical properties. As a result, it can preserve its structure after lyophilization. However, the low molecular weight is a detriment to long-term cell culturing, because the associated low pore size limits the diffusion of nutrients into the hydrogel.[59] If long-term cell culturing is required, other types of hydrogels, particularly those containing methacrylate groups, can be used to promote cell viability after encapsulation. We have found that visible-laser-induced photocrosslinking of VA-086 can also be used with methacrylate hydrogels and gelatin coatings to establish high cell viabilities with good cell adhesion.[50]

The proposed DLBP technique can also be modified to improve photoinitiation. In particular, photoinitiators other than VA-086 could be used to increase the efficiency (while monitoring cell viability after encapsulation). An example is lithium phenyl-2,4,6-trimethylbenzoylphosphinate (LAP).[60] There has been no comprehensive study to compare the cell viability after encapsulation

of the LAP and VA-086 photoinitiators, but LAP does not generate nitrogen gas during its initiation so it may generate less stress to the cells.

The proposed DLBP technique can also be modified according to spatial resolution requirements. Resolution in the transverse plane can be improved by decreasing the size of the laser beamspot to a micron-scale. Although not shown herein, this can be realized by using a microscope objective with a higher numerical aperture and longer working distance. The feature resolution in the vertical plane can be improved by applying this high-numerical-aperture microscope objective, which decreases the depth of focus, or by applying dye (e.g., Sudan Red G) in the focal plane so that photocrosslinking occurs predominantly within the focal plane.[61] It may also be possible to apply multiphoton absorption within a thin focal plane by employing femtosecond pulsed lasers. A preliminary study on the use of these pulsed lasers has recently been carried out.[62]

Table 1 gives a summary of the resolution, vertical fabrication capabilities, and cell viability of the proposed bioprinting technique with respect to contemporary bioprinting techniques. It is seen that DLBP is the only technique that can simultaneously provide high resolution, a vertical fabrication capability, and high cell viability. Some general comments on potential modifications to the technique are given in the remainder of this section.

In this study, we report a new DLBP system and demonstrate its use to create fine hydrogels structures. The DLBP system was realized by visible-laser-induced photocrosslinking at a wavelength of 405 nm with the photoinitiator VA-086. A systematic characterization was carried out on the photocrosslinking process. The DLBP system was shown to have a fine feature

resolution (being less than 50 μm), vertical fabrication capabilities, and excellent cell viability (being greater than 95%). The DLBP system was successfully applied to the fabrication of cell-laden hydrogel microgrids and hydrogel microwells. Finally, the DLBP system is a highly promising tool for tissue engineering applications – a field rapidly growing in importance for human health.

Materials and Methods

DLBP System setup

The experimental setup seen in Figure 1A uses a laser diode module (Armlaser, San Francisco, CA, USA) with a maximum power of 150 mW at a wavelength of 405 nm. A variable optical attenuator was installed below the laser, with a slight tilt between its surface normal and the laser beam to prevent reflective feedback into the laser. A screen was mounted above the laser (not shown) to protect users in the vicinity. The laser beam was focused by a 20× microscope objective into a Petri dish containing the PEGDA prepolymer solution. The Petri dish was mounted on a 50-mm lens holder that is attached to the actuation system. The actuation system uses three single-axis 25-mm motorized actuators (MTS25/M-Z8, Thorlabs Inc., Newton, NJ, USA), for x-, y- and z-motion control via LabVIEW (National Instruments Corp., Austin, TX, USA). A beam-block was placed beneath the Petri dish to block unabsorbed laser light.

Material preparation

Poly(ethylene glycol) diacrylate 700 Da (PEGDA) was purchased from Sigma Aldrich (St. Louis, MO, USA). The VA-086 photoinitiator was purchased from Wako Chemicals Inc. (Osaka, Japan).

The PEGDA prepolymer solution was prepared by dissolving 10% w/v PEGDA 700 solution and 1% w/v VA-086 photoinitiator in pH 7.4 phosphate-buffered saline (PBS) solution (Life Technologies, Carlsbad, CA, USA).

The chemically functionalized glass slides were prepared in a class-100 cleanroom facility to control dust and contamination. A glass slide (75 mm × 25 mm × 1 mm, VWR Scientific, Radnor, PA, USA) was cut into a square with dimensions of 25 mm × 25 mm × 1 mm and was treated by an oxygen plasma using a hand-held corona device (BS-20, Electro-Techni Products, Chicago, IL, USA). The treated square glass slide was then placed into a spincoater (WS-650 Spin Processor, Laurell Technol. Corp., North Wales, PA, USA) for coating with a thin layer of 3-(Trimethoxysilyl)propyl methacrylate (Sigma Aldrich, St. Louis, MO, USA) using 2000 rpm for 35 seconds. The 3-(Trimethoxysilyl)propyl methacrylate-coated square glass slide was then baked at 75ºC for 24 hours.

UV-Vis spectra

The absorption spectrum of the VA-086 photoinitiator was measured with a UV-visible spectrophotometer (UV-2550, Shimadzu, Kyoto, Japan). The results were normalized and presented as a function of wavelengths from 300 to 800 nm. The PEGDA prepolymer solution sample, containing 10% w/v PEGDA 700 solution and 1% w/v VA-086 photoinitiator, was prepared as described above. A blank PBS solution sample, containing only 10% w/v PEGDA 700 solution, was prepared and used as a reference spectrum.

Scanning electron microscope (SEM)

The bioprinted hydrogel patterns were characterized via SEM imaging. After bioprinting, the PEGDA prepolymer solution was removed from the Petri dish. The hydrogel patterns were carefully rinsed with PBS solution three times and stored in a freezer at -80°C for four hours. The hydrogel patterns were then taken out and placed in a freeze dryer for 24 hours of lyophilizing. The freeze dried hydrogel patterns were then stored in a freezer at -80°C before SEM observation. The samples were coated with 10-nm-thick gold-palladium layers and images were acquired with a SEM (Mira3 XMU, TESCAN, Brno, Czech Republic).

Cell culture, seeding, and encapsulation

The MCF-7 cells were cultured in an incubator at 37°C and 5% CO_2. The cell medium was made from Dulbecco's modified eagle medium (DMEM) consisting of 10% fetal bovine serum, 1% v/v penicillin-streptomycin, and 1% v/v amphotericin B (Life Technologies, Carlsbad, CA, USA). The cell medium was replaced every three days. For the fabrication of microwells, the hydrogel patterns were rinsed by the PBS solution three times after bioprinting. The MCF-7 cells (2×10^5 cells/mL) were then added to the Petri dish, and the hydrogel patterns were cultured for three days. The cell viability and proliferation were examined at day 3 by live/dead assay (Biotium Inc., Fremont, CA, USA) and confocal microscopy. For the fabrication of cell-laden hydrogel patterns, MCF-7 cells (2×10^6 cells/mL) were mixed with the PEGDA prepolymer solution. The cell viability was examined immediately after the bioprinting process via live/dead assay and confocal microscopy.

Confocal imaging and image-based analyses

The viability of the encapsulated MCF-7 cells was then tested immediately after bioprinting with a live/dead assay under a confocal microscope. The live/dead assay contains green calcein acetoxymethyl (Calcein AM) for live cells and red ethidium homodimer III (EthD-III) for dead cells. For the confocal imaging and image-based analyses, the hydrogel patterns were first rinsed by the PBS solution three times and then stained by the live/dead assay containing 2 µM of Calcein AM and 4 µM EthD III. After 30 minutes, the stained hydrogel patterns were rinsed twice by the PBS solution and immediately examined under the confocal microscope (FV1000, Olympus, Tokyo, Japan). A 10× microscope objective was used to observe the bioprinted samples. Olympus Fluoview (version 4.0) was employed to acquire fluorescence images and construct the results.

To quantify cell viability, the numbers of live and dead cells of the cell-laden hydrogel patterns were counted through a cell counting function provided by FIJI ImageJ (NIH, Bethesda, MD, USA). The cell viability was then calculated according to

$$\text{Cell viability} = \frac{\text{Number of live cells in the field of view}}{\text{Number of live and dead cells in the field of view}}.$$

To analyze cell confluency, the green channel of the fluorescence images at day 3 was processed. The fluorescence images were first converted to gray-scale images. A minimal intensity threshold was then set for the gray-scale images to select the bright pixels (i.e., the selected areas with sufficiently high brightness to indicate the presence of cells stained with Calcein AM). The cell confluency was then calculated according to

$$\text{Cell confluency} = \frac{\text{Number of bright pixels in the microwell}}{\text{Number of total pixels in the microwell}}.$$

To analyze the uniformity of the cell distribution, the quadrant method was used[58]. The green channel of the fluorescence images was first converted to create gray-scale images with a fixed threshold level (See Figures S3A and S3B). The area inside a microwell was then divided into a 3-by-3 grid to produce five quadrants: top-left (TL), top-right (TL), middle (M), bottom-left (BL), and bottom-right (BR) (See Figure S3C). Cell confluencies were then computed for the five quadrants using the method described above for cell confluency (See Figures S3D and S3E for representative cell confluencies). The uniformity of the cell distribution was then computed as an average of four cell-confluency ratios, according to

$$\text{Uniformity of the cell distribution} =$$
$$\frac{1}{4}\left(\frac{\text{M cell confluency}}{\text{TL cell confluency}} + \frac{\text{M cell confluency}}{\text{TR cell confluency}} + \frac{\text{M cell confluency}}{\text{BL cell confluency}} + \frac{\text{M cell confluency}}{\text{BR cell confluency}}\right)$$

(See Figure S3F for a representative uniformity of the cell distribution).

Statistical analysis

The experimental data (hydrogel line width, cell viability, cell confluency and uniformity) were plotted in the form of mean $\pm$ standard deviation. No pre-processing was performed. Sample sizes (n) of experimental data were indicated in the corresponding figure caption. One-way analysis of variance (ANOVA) test was used to derminine the statistical differences (p-value) of cell viability, cell confluency and uniformity. The statistical analysis was conducted using MATLAB 2015b.

Acknowledgements

Author contributions

Z.W. and X.J. designed and performed all experiments. Z.T. performed UV-Vis measurements. F.M. provided UV-Vis equipment. Z.T. and F.M. helped write manuscript. Z.W., X.J., J.F.H., and K.K. conceived the research, designed the experiments, and wrote the manuscript.

References

[1]   M. W. Tibbitt, K. S. Anseth, *Biotechnol. Bioeng.* **2009**, *103*, 655.

[2]   M. Ravi, V. Paramesh, S. R. Kaviya, E. Anuradha, F. D. Paul Solomon, *J. Cell. Physiol.* **2015**, *230*, 16.

[3]   K. M. Yamada, E. Cukierman, *Cell* **2007**, *130*, 601.

[4]   D. E. Discher, D. J. Mooney, P. W. Zandstra, *Science* **2009**, *324*, 1673.

[5]   M. P. Lutolf, P. M. Gilbert, H. M. Blau, *Nature* **2009**, *462*, 433.

[6]   F. M. Watt, W. T. S. Huck, *Nat. Rev. Mol. Cell Biol.* **2013**, *14*, 467.

[7]   S. Huang, D. E. Ingber, *Cancer Cell* **2005**, *8*, 175.

[8]   C. Fischbach, H. J. Kong, S. X. Hsiong, M. B. Evangelista, W. Yuen, D. J. Mooney, *Proc. Natl. Acad. Sci. U. S. A.* **2009**, *106*, 399.

[9]   D. Huh, G. A. Hamilton, D. E. Ingber, *Trends Cell Biol.* **2011**, *21*, 745.

[10]   D. Huh, B. D. Matthews, A. Mammoto, M. Montoya-Zavala, H. Y. Hsin, D. E. Ingber, *Science* **2010**, *328*, 1662.

[11]   S. V Murphy, A. Atala, *Nat. Biotechnol.* **2014**, *32*, 773.

[12]   H.-W. Kang, S. J. Lee, I. K. Ko, C. Kengla, J. J. Yoo, A. Atala, *Nat. Biotechnol.* **2016**, *34*, 312.

[13]   S. N. Bhatia, D. E. Ingber, *Nat. Biotechnol.* **2014**, *32*, 760.

[14]   Z. Wang, R. Samanipour, K. Kim, In *Biomedical Engineering: Frontier Research and Converging Technologies*; 2015; Vol. 9, pp. 209–233.

[15]   Š. Selimović, M. R. Dokmeci, A. Khademhosseini, *Curr. Opin. Pharmacol.* **2013**, *13*, 829.

[16]   F. Zheng, F. Fu, Y. Cheng, C. Wang, Y. Zhao, Z. Gu, *Small* **2016**, *12*, 2253.

[17]   H. Lee, D.-W. Cho, *Lab Chip* **2016**, *16*, 2618.

[18]   C. Mandrycky, Z. Wang, K. Kim, D. H. Kim, *Biotechnol. Adv.* **2015**, *34*, 422.

[19]   D. B. Kolesky, R. L. Truby, A. S. Gladman, T. A. Busbee, K. A. Homan, J. A. Lewis, *Adv. Mater.* **2014**, *26*, 3124.

[20]   L. E. Bertassoni, J. C. Cardoso, V. Manoharan, A. L. Cristino, N. S. Bhise, W. A. Araujo, P. Zorlutuna, N. E. Vrana, A. M. Ghaemmaghami, M. R. Dokmeci, A. Khademhosseini, *Biofabrication* **2014**, *6*, 24105.

[21]   L. E. Bertassoni, M. Cecconi, V. Manoharan, M. Nikkhah, J. Hjortnaes, A. L. Cristino, G. Barabaschi, D. Demarchi, M. R. Dokmeci, Y. Yang, A. Khademhosseini, *Lab Chip* **2014**, *14*, 2202.

[22]   D. B. Kolesky, K. A. Homan, M. A. Skylar-Scott, J. A. Lewis, *Proc. Natl. Acad. Sci.* **2016**, *113*, 3179.

[23]   W. Jia, P. S. Gungor-Ozkerim, Y. S. Zhang, K. Yue, K. Zhu, W. Liu, Q. Pi, B. Byambaa, M. R. Dokmeci, S. R. Shin, A. Khademhosseini, *Biomaterials* **2016**.

[24]   W. Liu, Y. S. Zhang, M. A. Heinrich, F. De Ferrari, H. L. Jang, S. M. Bakht, M. M. Alvarez, J. Yang, Y.-C. Li, G. Trujillo-de Santiago, A. K. Miri, K. Zhu, P. Khoshakhlagh, G. Prakash, H. Cheng, X. Guan, Z. Zhong, J. Ju, G. H. Zhu, X. Jin, S. R. Shin, M. R. Dokmeci, A. Khademhosseini, *Adv. Mater.* **2016**, 1.

[25]   L. Ouyang, C. B. Highley, W. Sun, J. A. Burdick, *Adv. Mater.* **2016**, 1604983.

[26]   S. Khalil, W. Sun, *Mater. Sci. Eng. C* **2007**, *27*, 469.

[27]   S. Khalil, W. Sun, *J. Biomech. Eng.* **2009**, *131*, 111002.

[28]   J. He, X. Zhao, J. Chang, D. Li, *Small* **2017**, *1702626*, 1702626.

[29]   X. Cui, D. Dean, Z. M. Ruggeri, T. Boland, *Biotechnol. Bioeng.* **2010**, *106*, 963.

[30]   G. Gao, T. Yonezawa, K. Hubbell, G. Dai, X. Cui, *Biotechnol. J.* **2015**, *10*, 1568.

[31]   B. Guillotin, A. Souquet, S. Catros, M. Duocastella, B. Pippenger, S. Bellance, R. Bareille, M. Rémy, L. Bordenave, J. Amédée, F. Guillemot, *Biomaterials* **2010**, *31*, 7250.

[32]   F. Guillemot, A. Souquet, S. Catros, B. Guillotin, J. Lopez, M. Faucon, B. Pippenger, R. Bareille, M. Remy, S. Bellance, P. Chabassier, J. C. Fricain, J. Amedee, *Acta Biomater.* **2010**, *6*, 2494.

[33]   S. Catros, J.-C. Fricain, B. Guillotin, B. Pippenger, R. Bareille, M. Remy, E. Lebraud, B. Desbat, J. Amédée, F. Guillemot, *Biofabrication* **2011**, *3*, 25001.

[34]   H. Lin, D. Zhang, P. G. Alexander, G. Yang, J. Tan, A. W. M. Cheng, R. S. Tuan, *Biomaterials* **2013**, *34*, 331.

[35]   A. X. Sun, H. Lin, A. M. Beck, E. J. Kilroy, R. S. Tuan, *Front. Bioeng. Biotechnol.* **2015**, *3*, 115.

[36]   R. Gauvin, Y. C. Chen, J. W. Lee, P. Soman, P. Zorlutuna, J. W. Nichol, H. Bae, S. Chen, A. Khademhosseini, *Biomaterials* **2012**, *33*, 3824.

[37]   J. Warner, P. Soman, W. Zhu, M. Tom, S. Chen, *ACS Biomater. Sci. Eng.* **2016**, *2*, 1763.

[38]   D. Karabacak, T. Kouh, C. C. Huang, K. L. Ekinci, *Appl. Phys. Lett.* **2006**, *88*, 193122.

[39]   A. Paguirigan, D. J. Beebe, *Lab Chip* **2006**, *6*, 407.

[40]   Y. Sakai, Y. Yoshiura, K. Nakazawa, *J. Biosci. Bioeng.* **2011**, *111*, 85.

[41]   J. M. Karp, J. Yeh, G. Eng, J. Fukuda, J. Blumling, K.-Y. Suh, J. Cheng, A. Mahdavi, J. Borenstein, R. Langer, A. Khademhosseini, *Lab Chip* **2007**, *7*, 786.

[42]   J. M. Cha, H. Bae, N. Sadr, S. Manoucheri, F. Edalat, K. Kim, S. B. Kim, I. K. Kwon, Y.-S. Hwang, A.

Khademhosseini, *Macromol. Res.* **2015**, *23*, 245.

[43]   Y. Y. Choi, B. G. Chung, D. H. Lee, A. Khademhosseini, J. H. Kim, S. H. Lee, *Biomaterials* **2010**, *31*, 4296.

[44]   Y.-C. Chen, X. Lou, Z. Zhang, P. Ingram, E. Yoon, *Sci. Rep.* **2015**, *5*, 12175.

[45]   U. P. Kappes, D. Luo, M. Potter, K. Schulmeister, T. M. Rünger, *J. Invest. Dermatol.* **2006**, *126*, 667.

[46]   C. G. Williams, A. N. Malik, T. K. Kim, P. N. Manson, J. H. Elisseeff, *Biomaterials* **2005**, *26*, 1211.

[47]   K. T. Nguyen, J. L. West, *Biomaterials* **2002**, *23*, 4307.

[48]   I. Mironi-Harpaz, D. Y. Wang, S. Venkatraman, D. Seliktar, *Acta Biomater.* **2012**, *8*, 1838.

[49]   A. D. Rouillard, C. M. Berglund, J. Y. Lee, W. J. Polacheck, Y. Tsui, L. J. Bonassar, B. J. Kirby, *Tissue Eng. Part C. Methods* **2011**, *17*, 173.

[50]   Z. Wang, X. Jin, R. Dai, J. F. Holzman, K. Kim, *RSC Adv.* **2016**, *6*, 21099.

[51]   C. Fischbach, R. Chen, T. Matsumoto, T. Schmelzle, J. S. Brugge, P. J. Polverini, D. J. Mooney, *Nat. Methods* **2007**, *4*, 855.

[52]   Y.-S. Hwang, B. G. Chung, D. Ortmann, N. Hattori, H.-C. Moeller, A. Khademhosseini, *Proc. Natl. Acad. Sci. U. S. A.* **2009**, *106*, 16978.

[53]   J. C. Mohr, J. J. de Pablo, S. P. Palecek, *Biomaterials* **2006**, *27*, 6032.

[54]   R. El Assal, U. A. Gurkan, P. Chen, F. Juillard, A. Tocchio, T. Chinnasamy, C. Beauchemin, S. Unluisler, S. Canikyan, A. Holman, S. Srivatsa, K. M. Kaye, U. Demirci, *Sci. Rep.* **2016**, *6*, 39144.

[55]   M. Charnley, M. Textor, A. Khademhosseini, M. P. Lutolf, *Integr. Biol. (Camb).* **2009**, *1*, 625.

[56]   A. H. Broderick, S. M. Azarin, M. E. Buck, S. P. Palecek, D. M. Lynn, *Biomacromolecules* **2011**, *12*, 1998.

[57]   L. Kang, M. J. Hancock, M. D. Brigham, A. Khademhosseini, *J. Biomed. Mater. Res. - Part A* **2010**, *93*, 547.

[58]   K. M. Kam, L. Zeng, Q. Zhou, R. Tran, J. Yang, *J. Manuf. Syst.* **2013**, *32*, 154.

[59]   V. Chan, P. Zorlutuna, J. H. Jeong, H. Kong, R. Bashir, *Lab Chip* **2010**, *10*, 2062.

[60]   B. D. Fairbanks, M. P. Schwartz, C. N. Bowman, K. S. Anseth, *Biomaterials* **2009**, *30*, 6702.

[61]   M. P. Lee, G. J. T. Cooper, T. Hinkley, G. M. Gibson, M. J. Padgett, L. Cronin, *Sci. Rep.* **2015**, *5*, 9875.

[62]   K. C. Hribar, K. Meggs, J. Liu, W. Zhu, X. Qu, S. Chen, *Sci. Rep.* **2015**, *5*, 17203.

[63]   J. Phillippi, E. Miller, L. Weiss, J. Huard, A. Waggoner, P. Campbell, *Stem Cells* **2008**, *26*, 127.

[64]   I. T. Ozbolat, M. Hospodiuk, *Biomaterials* **2016**, *76*, 321.

Table

Table 1. Comparison of the resolution, vertical fabrication capabilities, and cell viability of contemporary bioprinting techniques and the proposed DLBP technique.

	Inkjet	LIFT	Extrusion	Stereolithography	DLBP
Resolution	50 μm	100 μm	> 200 μm 80 μm (Alginate)	500 μm (Visible light) 50 μm (UV)	50 μm (Visible light)
Structural integrity	Poor	Fair	Good	Good	Good
Cell viability	> 85%	> 95%	40% - 80%	90%	95%
References	[18,29,30,63]	[18,31,33]	[18,19,24,25,28,64]	[34–37]	This work

Figures
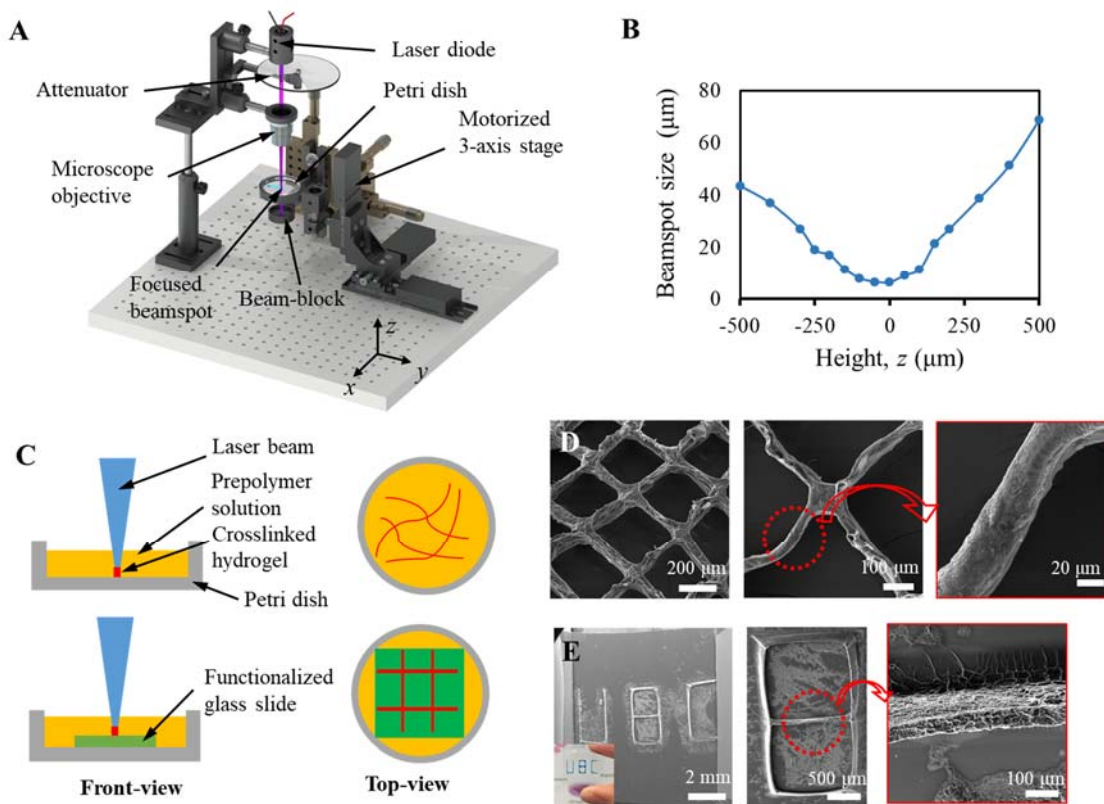
Figure 1. Characterization of the direct laser bioprinting (DLBP) system. (A) 3D schematic of the system. (B) Characterization of the laser beamspot size as a function of the height along the z-axis. (C) Schematics of the bioprinting process for freestanding hydrogel patterns (upper) and the fixed hydrogel patterns on a methacrylated glass slide (bottom). (D) SEM images of a freestanding hydrogel pattern in the form of a grid. (Scale bar = 200 μm) (E) SEM images of a fixed hydrogel pattern in the form of 'UBC'.
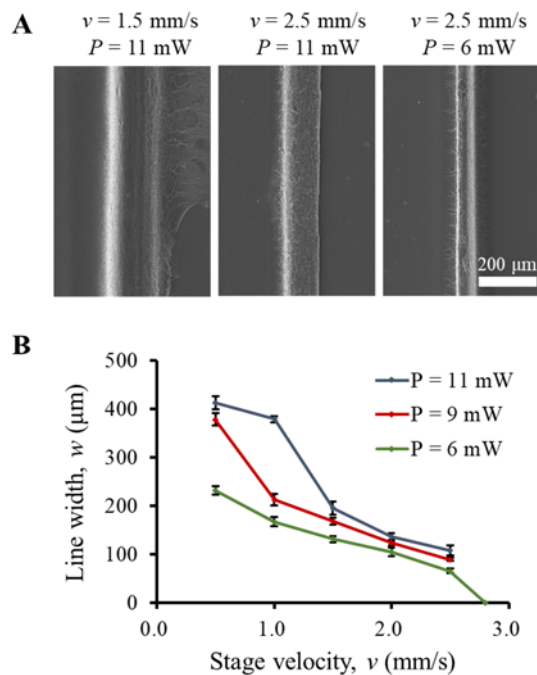
Figure 2. Measurements are shown for the hydrogel lines as a function of the stage velocity and optical power. (A) Representative SEM images of hydrogel lines with stage velocities and optical powers of $v = 1.5$ mm/s and $P = 11$ mW, $v = 2.5$ mm/s and $P = 11$ mW, and $v = 2.5$ mm/s and $P = 6$ mW. (B) Measured hydrogel line width, w, as a function of the stage velocity, v, for optical powers of $P = 6, 9,$ and 11 mW ($n = 5$).
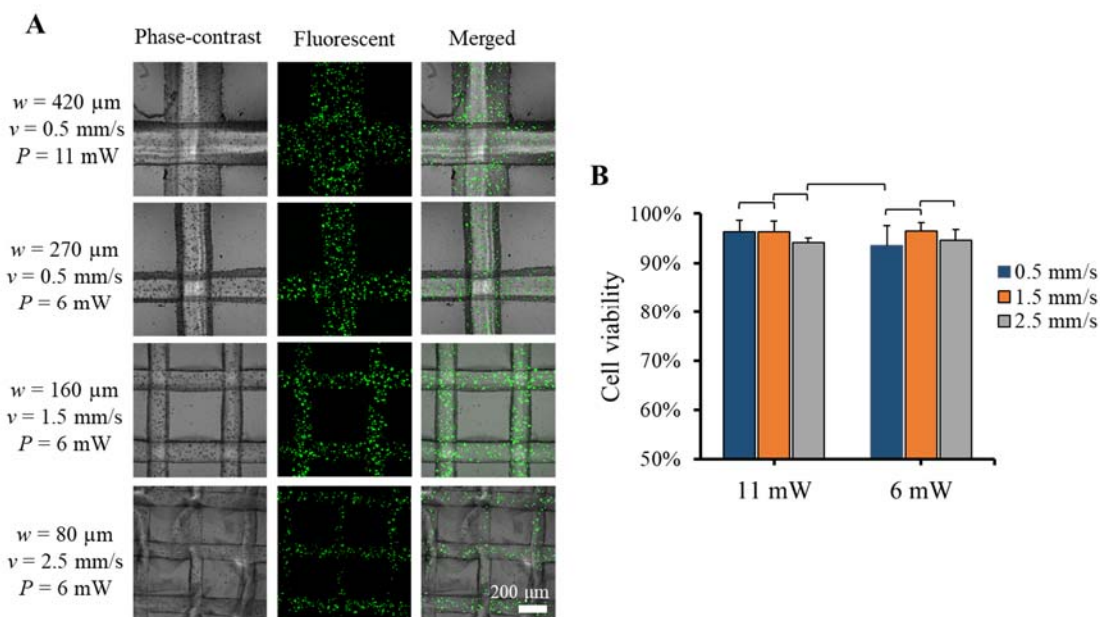
Figure 3. Bioprinting of cell-laden hydrogel microgrids using the DLBP system. (A) Fluorescence images of MCF-7 cell-laden microgrids given differing stage velocities and optical powers for the fabrication. (B) Results for the cell viability at Day-0 for cell-laden hydrogel microgrids being fabricated with differing stage velocities and optical powers ($n = 5$). The statistical results show that there is no statistical significance between two samples ($p > 0.05$).
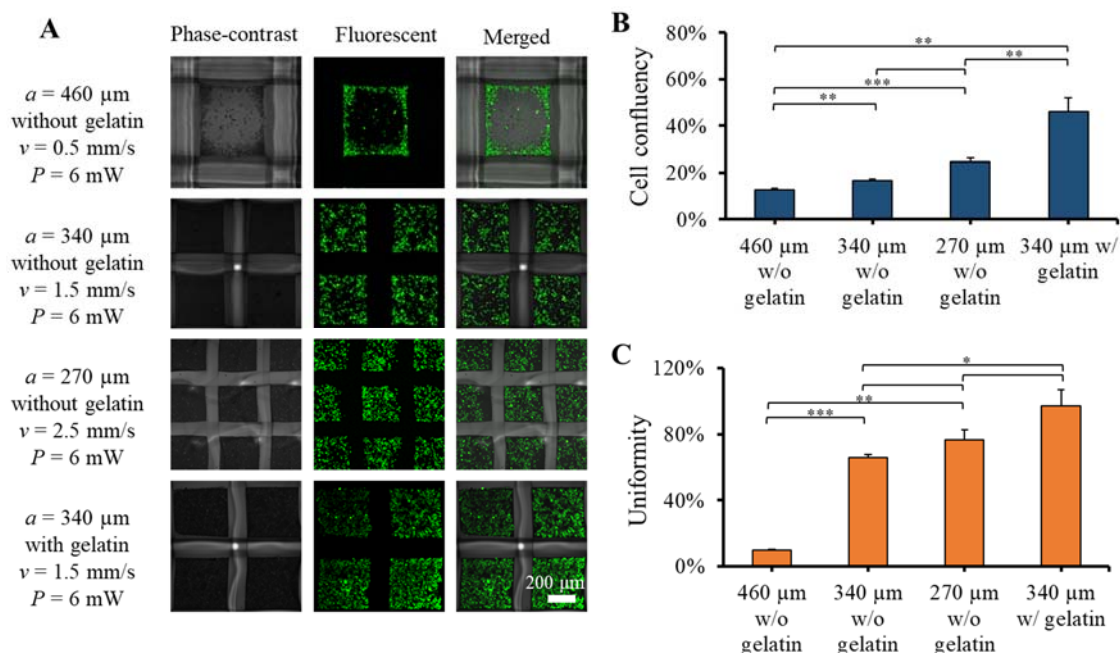
Figure 4. Bioprinting of hydrogel microwells using the DLBP system. (A) Fluorescence images of MCF-7 cells in hydrogel microwells having differing side-lengths with and without the gelatin coating. (B) Results for the cell confluency for hydrogel microwells having differing side-lengths with and without the gelatin coating (n = 3, 8, and 27 for 460, 340, and 270 μm microwells, respectively, **$p < 0.01$, and ***$p < 0.001$). (C) Results for the uniformity of cell distribution for hydrogel microwells having differing side-lengths with and without the gelatin coating (n = 3, 8, and 27 for 460, 340, and 270 μm microwells, respectively, *$p < 0.05$, **$p < 0.01$, and ***$p < 0.001$).
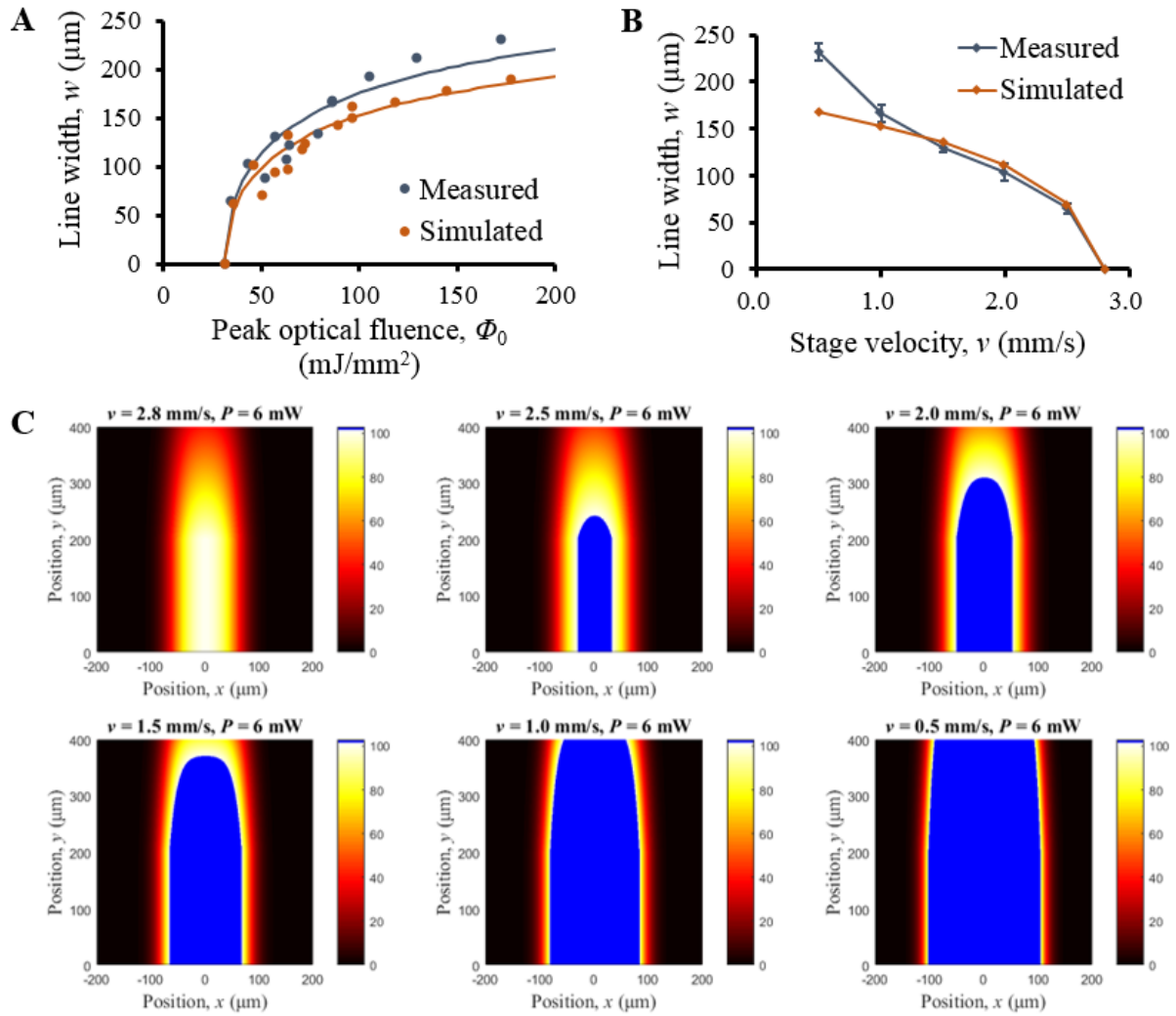
Figure 5. Measurements and simulations are shown for the hydrogel lines as a function of the stage velocity and optical power. (A) Measured and simulated hydrogel line width, w, as a function of the stage velocity, v, for an optical power of $P = 6$ mW. (B) Measured and simulated hydrogel line width, w, as a function of the peak optical fluence, Φ_0, for an optical power of $P = 6$ mW. (C) Simulations of the concentration of polymer chains, $[N(x,y,t)]$, as a normalized colourmap (out of 100) for the laser beamspot traveling along the y-axis while centered about $x = 0$. The stage velocities are $v = 2.8$, 2.5, 2.0, 1.5, 1.0, and 0.5 mm/s. The optical power is 6 mW. Areas that are above the threshold concentration of $[N_{th}] = 100$ are shown in blue. These blue areas have undergone sufficient polymerization to form the hydrogel line.
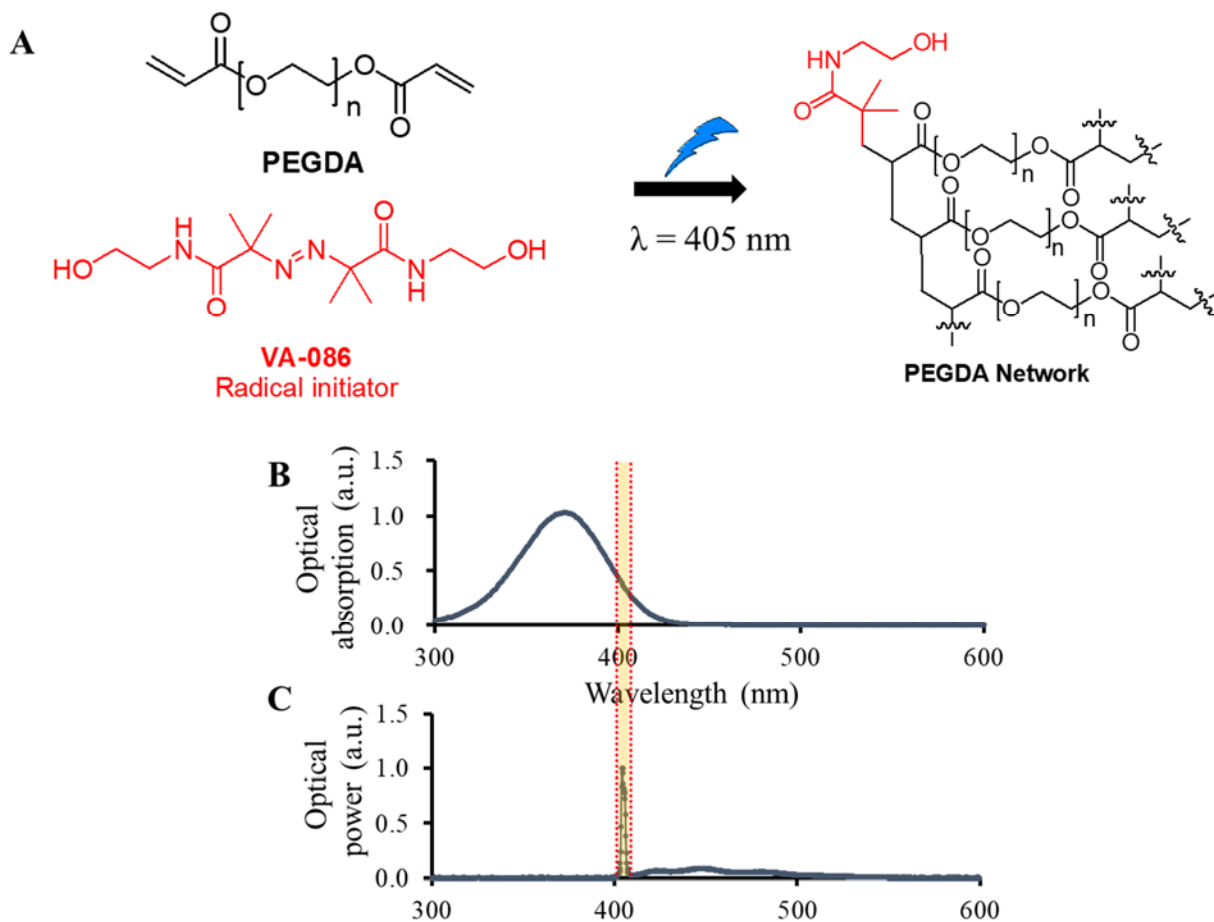
Figure 6. Photocrosslinking of the VA-086 photoinitiator. (A) Formation of the PEGDA hydrogel network in the presence of free radicals (having been generated by the VA-086 photoinitiator). (B) UV-visible spectra of the VA-086 photoinitiator. Peak absorption occurs at approximately 370 nm, but significant absorption (greater than 30%) occurs at 405 nm. (C) Spectrum of the visible (GaN-based) laser diode that is used for photocrosslinking.